PHYSICAL REVIEW A **88**, 052505 (2013)

Satellite and hypersatellite structures of $L\alpha_{1,2}$ and $L\beta_1$ x-ray transitions in mid-Z atoms multiply ionized by fast oxygen ions

M. Czarnota,[1,*] D. Banaś,[1] M. Berset,[2] D. Chmielewska,[3] J.-Cl. Dousse,[2] J. Hoszowska,[2] Y.-P. Maillard,[2] O. Mauron,[2] M. Pajek,[1] M. Polasik,[4] P. A. Raboud,[2] J. Rzadkiewicz,[5] K. Słabkowska,[4] and Z. Sujkowski[3,†]
[1]*Institute of Physics, Jan Kochanowski University, 25-406 Kielce, Poland*
[2]*Department of Physics, University of Fribourg, CH-1700 Fribourg, Switzerland*
[3]*Sołtan Institute for Nuclear Studies, 05-400 Otwock-Świerk, Poland*
[4]*Faculty of Chemistry, Nicholas Copernicus University, 87-100 Toruń, Poland*
[5]*National Centre for Nuclear Research, 05-400 Otwock-Świerk, Poland*

(Received 15 June 2013; published 11 November 2013)

A detailed investigation of the $L\alpha_{1,2}$ ($L_3 \rightarrow M_{4,5}$) and $L\beta_1$ ($L_2 \rightarrow M_4$) x-ray satellite and hypersatellite structures in zirconium, molybdenum, and palladium atoms multiply ionized by impact with 278.6-MeV oxygen ions is reported. The x-ray spectra were measured with a high-resolution von Hamos bent crystal spectrometer. For the interpretation of the complex spectral features, relativistic multiconfiguration Dirac-Fock calculations were performed for all multivacancy configurations expected to contribute to the observed spectra. The data analysis clearly demonstrates that the spectra are dominated by structures originating from ($L^{-1}M^{-m}N^{-n}$) satellite and ($L^{-2}M^{-m}N^{-n}$) hypersatellite transitions corresponding to the radiative decay of the excited multivacancy configurations. The ionization probabilities of the L and M shell were determined from the data and compared with theoretical predictions from the geometrical model and the semiclassical approximation, using in the latter case both relativistic hydrogenlike and self-consistent Dirac-Hartree-Fock wave functions. The results support the independent electron picture of the multiple ionization. They also show the importance of using relativistic and self-consistent electronic wave functions for the L and M shells.

DOI: 10.1103/PhysRevA.88.052505 PACS number(s): 32.30.Rj, 34.50.Fa, 32.70.Jz, 32.80.Hd

I. INTRODUCTION

The observation of the x-ray diffraction by crystals opened up a new technique with unprecedented precision for the study of x rays, namely the high-resolution x-ray spectroscopy. Soon after, Siegbahn and Stenström [1] discovered new lines in K x-ray spectra. The latter, whose energies did not correspond to any diagram x-ray transition, were named *satellite* x-ray lines. They were found to appear when additional vacancies that are not directly involved in the atomic transition are present during the x-ray emission. In this case, due to the reduced screening of the nuclear charge and resulting increase of the electron binding energies, the emitted *satellite* x rays have slightly higher energies than the common *diagram* transitions corresponding to the decay of single vacancies. The energy shift is the largest when in the initial state the two vacancies are located in the same shell. In this case the emitted x rays are called *hypersatellites* [2]. While the first observation of K- and L-shell hypersatellites were reported a long time ago [3–5], the final interpretation of their origin was given much later by Charpak [6] and Briand *et al.* [2,7].

The x-ray satellites and hypersatellites studied in the early days of x-ray spectroscopy (see Ref. [5]) were excited mainly by photon and electron impact. In this case, the double ionization of the target atoms is created via two-step processes. For the K shell the second vacancy is produced mainly by a shake process [8,9] which results from the sudden change of the atomic potential following the ionization of the first electron, or by the electron knockout by the first electron released in the photoionization process (see Refs. [10,11]). For the L shell the double vacancy states originate predominantly from auto-ionizing Auger [12] or Coster-Kronig [13] transitions. As a consequence, the double inner-shell ionization of atoms induced by photon and electron impact is rather weak. In contrast to that, x-ray satellites and hypersatellites with markedly higher intensities can be expected in x-ray spectra corresponding to collisions of atoms with heavy ions. Due to the strong Coulomb field of the projectile, several inner-shell electrons of the target atom can be indeed ionized simultaneously. Thus, x-ray spectra induced by heavy ion impact exhibit usually rich satellite and hypersatellite structures. The use of high-energy resolution instruments such as crystal spectrometers which is mandatory to unravel such complex x-ray spectra permits us to study both the *structure* of multivacancy states in atoms and the *dynamics* of the multiple ionization process.

The first high-resolution studies of x-ray satellites excited by ion impact are summarized in Ref. [14]. In particular, the first observation of the $K\alpha$ x-ray hypersatellites produced in ion-atom collisions was reported by Richard *et al.* [15]. Such measurements of heavy-ion induced K-hypersatellites were found to be a sensitive tool for studying the relativistic and quantum electrodynamics (QED) effects in atoms [16] and the dynamics of the multiple ionization of atoms by heavy-ion impact [17–19]. The observation of heavy-ion induced L-shell hypersatellites and their interpretation in terms of MCDF calculations were reported only recently [20,21].

A detailed knowledge of the satellite structure of the x rays emitted from multiply ionized atoms is of great interest in many domains. For instance, such knowledge is needed

---

[*] Present address: Faculty of Computer Science, Radom Academy of Economics, 26-600 Radom, Poland.

[†] Deceased.

for the interpretation of the extreme ultraviolet (EUV) and x-ray radiation from the Universe [22], for plasma diagnostics [23], for the development of new schemes for EUV and x-ray sources [24], as well as for applications of the x-ray free-electron lasers (XFELs) [25]. In particular, the interpretation of the complex structure of x-ray satellites is crucial for the studies of the formation of "hollow" atoms in collisions of slow highly charged ions (HCIs) with surfaces [26,27] and for the understanding of the x-ray emission from the matter irradiated by intense x-ray beams from XFELs [25,28].

In the present paper high-resolution measurements of the $L\alpha_{1,2}$ ($L_3 \rightarrow M_{5,4}$) and $L\beta_1$ ($L_2 \rightarrow M_4$) x-ray emission from selected mid-Z elements, namely zirconium, molybdenum, and palladium, bombarded by fast oxygen ions having an incident kinetic energy of about 280 MeV, are reported. The experimental data, interpreted in terms of the relativistic multiconfiguration Dirac-Fock (MCDF) calculations, reveal that the observed x-ray spectra have complex structures characterized by numerous and partly overlapping x-ray satellite and hypersatellite lines. We present here systematic investigation of L-shell x-ray hypersatellite transitions in mid-Z elements, while some preliminary results concerning palladium were already presented earlier in shorter papers [20,21]. In general, the observed fine details of the measured x-ray satellite and hypersatellite x-ray spectra are important to probe the goodness of atomic structure calculations [29]. In particular, high-resolution x-ray spectra such as those presented in this paper permit us to check the theoretical predictions from relativistic multiconfiguration Dirac-Fock (MCDF) calculations [30,31] including the Breit and QED corrections [32,33].

The paper is organized as follows. The experiments are described in Sec. II, which is followed by a presentation of the multiple ionization process (Sec. III) and the multiconfiguration Dirac-Fock calculations (Sec. IV). The analysis of the measured x-ray spectra in terms of the MCDF calculations is discussed in Sec. V, while the x-ray emission from the multiply ionized atoms and the vacancy rearrangement processes needed to interpret properly the observed intensities of the x-ray satellites are presented in Sec. VI. Finally, the ionization probabilities extracted from our data and their comparison with theoretical predictions as well as the conclusions of our study are given in Secs. VII and VIII, respectively.

II. EXPERIMENT

The present x-ray experiments were carried out at the Paul Scherrer Institute (PSI), in Villigen, Switzerland, using O^{6+} ions produced by a 10-GHz CAPRICE ECR ion source. The ions were accelerated to the final energy of 278.6 MeV by the variable energy Philips cyclotron of PSI. The x-ray spectra were measured with a high-resolution Bragg-type von Hamos bent crystal spectrometer. Thin metallic foils with thicknesses of 1.30 mg/cm^2 for zirconium, 2.56 mg/cm^2 for molybdenum, and 1.80 mg/cm^2 for palladium were used. The ion beam was focused on the targets to a 4-mm-high × 1-mm-wide spot. The intensity of the ion beam which was in the range 100–200 nA was monitored by observing the L-x-ray fluorescence from the studied targets by means of a Si PIN photodiode.

A. von Hamos spectrometer

The von Hamos–type crystal spectrometer [34] was built at the Physics Department of the University of Fribourg. The spectrometer is a compact high-energy resolution instrument contained in a stainless-steel high vacuum chamber that can be pumped down to 10^{-7} Torr by a turbomolecular pump. It consists mainly of a target holder, a slit system, a cylindrically bent crystal, and a charge-coupled device (CCD) camera for the detection of the diffracted x-ray photons (see Fig. 1). All movable parts of the spectrometer are operated by remotely controlled stepping motors.

The fluorescence x rays from the target were collimated by a tantalum slit defining the effective x-ray source size. For the present measurements a slit width of 0.2 mm was employed and the spectrometer was equipped with a 100-mm-high × 50-mm-wide × 0.15-mm-thick SiO_2 $(1\bar{1}0)$ crystal cylindrically bent to a radius of 25.4 cm. The diffracted x rays were measured with a two-dimensional position-sensitive CCD detector having a length of 28 mm and consisting of 256 × 1024 pixels with a pixel size of 27 μm. The CCD chip was cooled down to a working temperature of about $-60\,^{\circ}$C by means of Peltier elements. Due to the limited crystal length the x-ray energy range that could be measured with a given position of the crystal and detector was about 60 eV. Consequently, to measure the x-ray spectra over wider energy ranges up to six different crystal-detector settings were needed.

The energy calibration of the spectrometer was performed by measuring the $K\alpha_{1,2}$ and $L\beta_1$ lines of selected samples, using an x-ray tube for the production of the sample fluorescence. In order to cover the x-ray energy range of interest the $K\alpha_{1,2}$ lines from thin metallic foils of $_{21}$Sc, $_{23}$V, and $_{26}$Fe as well as the $L\beta_1$ lines of the investigated elements (Zr, Mo, and Pd) were employed. The absolute energy calibration of the spectrometer was done by adopting for the above transitions the energies quoted in [35], which resulted in uncertainties of about 0.3 eV for the energy calibration of the heavy-ion induced spectra. The x-ray tube measurements were also used to determine the energy resolution of the spectrometer. The

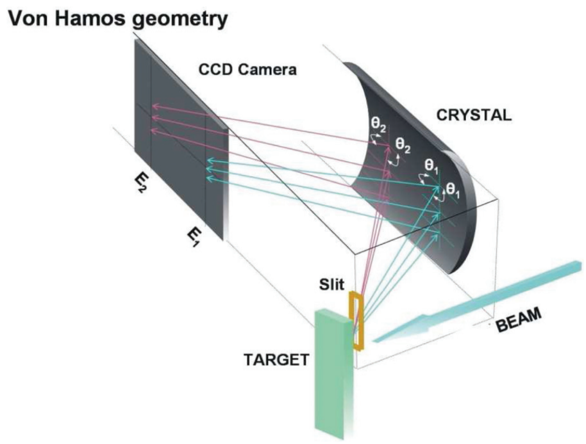

FIG. 1. (Color online) Schematic view of the working principle of the von Hamos spectrometer. The x rays diffracted by the cylindrically bent crystal are focused on the CCD camera at various positions depending on the energy of the photons.

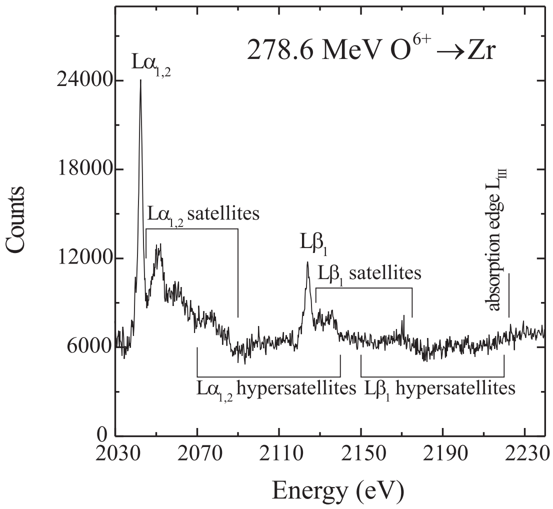

FIG. 2. Measured $L\alpha_{1,2} + L\beta_1$ x-ray spectrum of Zr resulting from the bombardment of the sample with 278.6 MeV O ions. The diagram x-ray transitions, the satellite and hypersatellite regions as well as the position of the L_3-absorption edge are indicated.

latter was found to vary between 0.3 and 0.6 eV for the $L\alpha_{1,2}$ and $L\beta_1$ x-ray lines of $_{40}$Zr, $_{42}$Mo, and $_{46}$Pd.

B. X-ray spectra

The heavy-ion induced x-ray spectra of Zr, Mo and Pd consisted of five to six regions, about 60 eV wide. For each target, the crystal and detector positions were chosen so that two adjacent regions were overlapping by about 10%. Off-line corrections were applied to each region to account for the small fluctuations of the beam intensity and beam profile on the target, the variation of the solid angle of the spectrometer which depends on the Bragg angle, and the self-absorption of the fluorescence x rays in the target. The reliability of the corrections was probed by comparing the partial spectra in the overlapping regions. From the comparison the precision of the absolute x-ray energy and relative intensity of the measured spectra was estimated to be 0.38 eV and 5%, respectively. The so-obtained $L\alpha_{1,2}$ and $L\beta_1$ x-ray spectra of Zr, Mo, and Pd are shown in Figs. 2–4, respectively.

III. MULTIPLE IONIZATION BY ION IMPACT

In multiple ionization by ion impact several electrons can be removed simultaneously from an atom due to their interaction with the Coulomb field of the incoming ion. Assuming the independent electron model in which one-electron ionization events can be considered as statistically independent, the probability of multiple ionization can be conveniently calculated in terms of the ionization probability per electron. Furthermore, the ionization probability per electron can be determined as a function of the impact parameter using the binary encounter approximation (BEA) based "geometrical model" [36,37] and the semiclassical approximation (SCA) [38,39].

A. Independent particle model

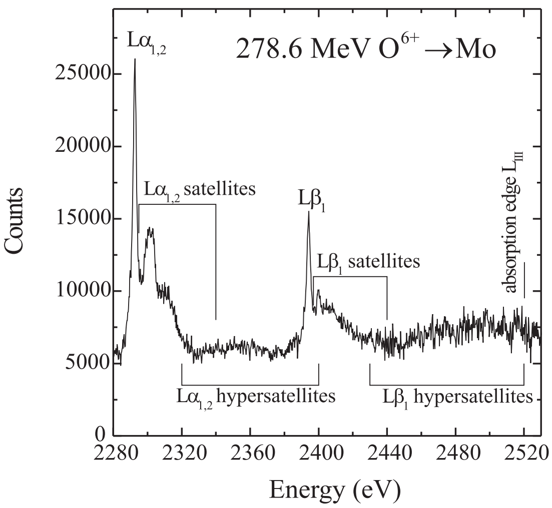

FIG. 3. Same as Fig. 2 but for molybdenum.

In this approximation, the interactions between the electrons are neglected and the electrons are therefore considered independent. Consequently, the single ionization probabilities can be determined from one-electron wave functions and the probability for removing several electrons is given by the product of the corresponding one-electron probabilities [40]. Assuming furthermore that the ionization probabilities are the same for all electrons belonging to the same shell, the probability for the creation of n vacancies in a shell containing N electrons can be expressed by a binomial distribution as follows:

$$P_n^N(b) = \binom{N}{n} p(b)^n [1 - p(b)]^{N-n}, \tag{1}$$

where $p(b)$ is the impact parameter dependent ionization probability per electron.

The probability for the creation of a $L^{-l}M^{-m}N^{-n}$ multivacancy state is then given by

$$P_{lmn}^{N_L N_M N_N}(b) = \binom{8}{l}\binom{18}{m}\binom{32}{n} p_L(b)^l [1 - p_L(b)]^{8-l} p_M(b)^m \times [1 - p_M(b)]^{18-m} p_N(b)^n [1 - p_N(b)]^{32-n}, \tag{2}$$

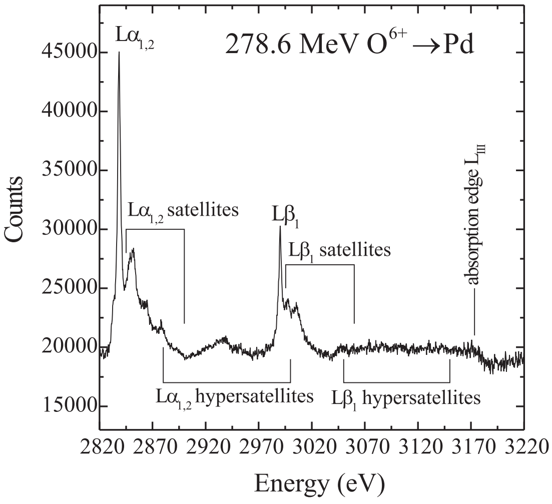

FIG. 4. Same as Fig. 2 but for palladium.

where $p_L(b)$, $p_M(b)$, and $p_N(b)$ are the ionization probabilities per electron for the L, M, and N shell filled initially with $N_L = 8$, $N_M = 18$, and $N_N = 32$ electrons, respectively.

B. Geometrical model

The geometrical model (GM), which was developed by Sulik *et al.* [37,41] to describe the ionization process in central collisions, i.e., in collisions corresponding to an impact parameter equal to zero, is based on the binary encounter approximation (BEA) [36,42]. In this model the ionization is treated as a classical collision between the charged projectile and the bound electron. The latter is removed from the atom when the energy transfer exceeds it binding energy, the momentum distribution of the electron in the initial bound state being described quantum mechanically by its wave function.

In this approach the ionization probability per electron for central collisions can be expressed by the universal BEA scaling parameter X_{nl} defined as follows [36,37]:

$$X_{nl} = 4(Z_1/v_1)V\sqrt{G_{nl}(V)}, \tag{3}$$

where Z_1 denotes the atomic number of the projectile and $V = v_1/v_2$ is the ratio of the projectile velocity to the effective electron velocity in the nl state. The universal function $G_{nl}(V)$ can be found in Ref. [36]. Using this scaling the BEA ionization probability per electron $p_{nl}(0,X_{nl})$ for an impact parameter equal to zero and a given hydrogenic nl state can be calculated as described in Ref. [37].

C. Semiclassical approximation

In the semiclassical approximation the ionization probability $p(b)$ as the function of the impact parameter b is described in terms of squared amplitudes of the electronic transitions from the initial to final states ($i \to f$) integrated over the electron final energies [38]:

$$p(b) = \int_0^{E_{\max}} \left[\hbar^{-1}\int_{-\infty}^{+\infty} dt\, e^{i(E_i-E_f)t/\hbar} \times \langle\psi_i|V(\mathbf{R}(b,t),r)|\psi_f\rangle\right]^2 dE_f, \tag{4}$$

where E_i and E_f are the electron energies in the initial and final states, $\mathbf{R}(b,t)$ describes the classical projectile trajectory, and ψ_i and ψ_j are the electron wave functions in the bound initial and continuum final states.

In the SCA approach the ionization probability given by Eq. (4) can be calculated [38,39] using hyperbolic projectile trajectories and electron hydrogenic relativistic wave functions (HYD) [43,44] or self-consistent Dirac-Hartree-Fock wave functions (DHF) [45,46]. Both HYD and DHF wave functions were used to interpret the x-ray satellite and hypersatellite spectra discussed in the present paper. As an example, the impact parameter dependence of the L- and M-shell ionization probabilities for molybdenum bombarded by oxygen ions is shown in Figs. 5 and 6, respectively. The probabilities were calculated within the SCA model using DHF wave functions because the latter give a more realistic description of the electronic wave functions than the hydrogenlike ones.

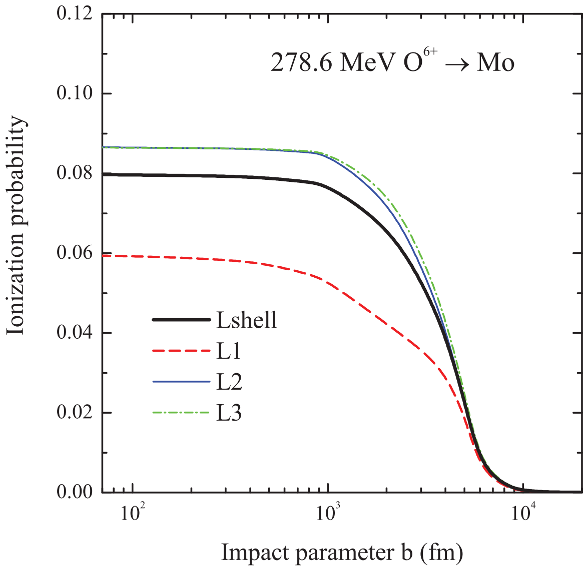

FIG. 5. (Color online) Dependence of the ionization probability per electron $p(b)$ on the impact parameter b for the L subshells and L shell of molybdenum. The ionization probabilities were calculated within the SCA approximation using relativistic Dirac-Hartree-Fock wave functions (DHF).

IV. MULTICONFIGURATION DIRAC-FOCK METHOD

To reproduce in detail the shapes of the complex satellite and hypersatellite x-ray spectra excited in collisions of atoms with heavy ions, multiconfiguration Dirac-Fock (MCDF) calculations are needed. Such calculations permit us indeed to determine both the energies and relative intensities of the x-ray multiplets corresponding to a given principal quantum number n, angular momentum l, and different values of the total angular momentum J. In general, the satellite and hypersatellite structures of x-ray transitions can be described by linear combinations of calculated MCDF transitions for each initial multivacancy configuration nlJ. As shown in

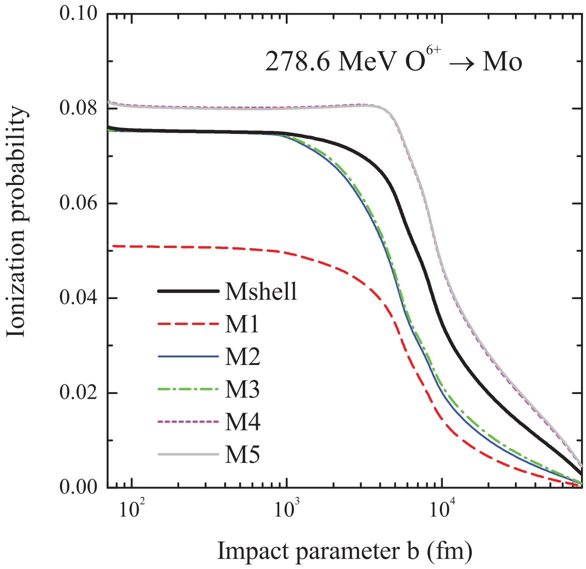

FIG. 6. (Color online) Same as Fig. 5 but for the Msubshells and M shell of molybdenum.

TABLE I. Number of transitions calculated within the MCDF model for various diagram, satellite and hypersatellite x-ray lines of zirconium, molybdenum and palladium. The configurations denoted "not calculated" were too complicated to be treated in the present calculations.

	Target		
Lines	Zr	Mo	Pd
Diagram lines			
$2p^{-1} \rightarrow 3d^{-1}$	3	3	3
N-shell satellites			
$2p^{-1}N^{-1} \rightarrow 3d^{-1}N^{-1}$	87	87	210
$2p^{-1}N^{-2} \rightarrow 3d^{-1}N^{-2}$	660	660	6157
M-shell satellites			
$2p^{-1}M^{-1} \rightarrow 3d^{-1}M^{-1}$	147	147	147
$2p^{-1}M^{-1}N^{-1} \rightarrow 3d^{-1}M^{-1}N^{-1}$	4438	4428	11600
$2p^{-1}M^{-2} \rightarrow 3d^{-1}M^{-2}$	3014	3013	3014
$2p^{-1}M^{-2}N^{-1} \rightarrow 3d^{-1}M^{-2}N^{-1}$	96793	96601	268210
$2p^{-1}M^{-3} \rightarrow 3d^{-1}M^{-3}$	34541	34572	34588
$2p^{-1}M^{-4} \rightarrow 3d^{-1}M^{-4}$	not calculated	not calculated	244953
L-shell hypersatellites			
$2p^{-1}L^{-1} \rightarrow 3d^{-1}L^{-1}$	45	45	45
$2p^{-1}L^{-1}N^{-1} \rightarrow 3d^{-1}L^{-1}N^{-1}$	not calculated	not calculated	3272
$2p^{-1}L^{-1}M^{-1} \rightarrow 3d^{-1}L^{-1}M^{-1}$	2253	2246	2249
$2p^{-1}L^{-1}M^{-2} \rightarrow 3d^{-1}L^{-1}M^{-2}$	48360	48098	48318
$2p^{-1}L^{-1}M^{-3} \rightarrow 3d^{-1}L^{-1}M^{-3}$	not calculated	not calculated	548391
Total	190341	189900	1171157

Table I the number of possible configurations grows rapidly with the number of additional vacancies and is especially high for atoms with open outer shells.

The MCDF calculations, which have been used in the present work, were described in detail in Refs. [31,47–49] so that, hereafter, only the most important features of the MCDF approach will be briefly reviewed. In the MCDF method a system of N electrons is described by the effective Hamiltonian

$$H = \sum_{i=1}^{N} h_D(i) + \sum_{j>i=1}^{N} C_{ij}, \tag{5}$$

where $h_D(i)$ is the Dirac operator for the ith electron:

$$h_D(i) = c\alpha \cdot p_i + (\beta - 1)m_e c^2 + V_{\text{nuc}}(r_i). \tag{6}$$

In Eq. (6) c represents the speed of light in vacuum, α and β are the Dirac matrices, p_i is the electron momentum, and $V_{\text{nuc}}(r_i)$ is the Coulomb potential $V_{\text{nuc}}(r_i) = -Ze^2/r_i$.

The $C_{ij} = 1/r_{ij} + T(r_{ij})$ operators describe the interaction between electrons via a virtual photon exchange, $1/r_{ij}$ and $T(r_{ij})$ standing for the Coulomb and Breit operators, respectively. The Breit operator reads as follows [32,33]:

$$T(r_{ij}) = \frac{-\alpha_i \cdot \alpha_j}{r_{ij}} + (\alpha_i \cdot \nabla_i)(\alpha_j \cdot \nabla_j)\frac{cos(\omega r_{ij}) - 1}{\omega^2 r_{ij}}, \tag{7}$$

where ω is the frequency of the photon exchanged in the interaction.

In the MCDF calculations the wave functions with the total angular momentum J and the parity p can be expressed as

$$\psi_s(J^p) = \sum_{m}^{N_c} c_m(s)\phi(\gamma_m J^p), \tag{8}$$

where s denotes the considered atomic state, $\phi(\gamma_m J^p)$ are the wave functions of different configurations with a total angular momentum J and a parity p, N_c is the number of all atomic configurations taken into account, $c_m(s)$ are the coefficients of the hybrid configurations for the state s and γ_m stands for the remaining quantum numbers.

In this work the MCDF calculations were performed using the modified special average-level version (MCDF-MSAL) proposed in [49,50]. In the calculations, in addition to the transverse (Breit) interaction, two types of QED energy corrections were taken into consideration, namely the self-energy and vacuum polarization, which are both significant in the case of heavy atoms [30,51–54]. The formulas for the transition matrix elements and spontaneous emission probabilities can be found in the work of Grant [55]. Some test calculations were performed using both the Coulomb and Babushkin [55,56] gauges. Despite the fact that the absolute line intensities depend slightly on the chosen gauge (which reflects the approximate character of the applied theoretical model), the structures of the groups of lines and the shapes of the whole theoretical spectra were found to be nearly insensitive to the choice of the gauge. Thus we decided to use in this work only the Coulomb gauge.

In the MCDF approach the x-ray transitions are calculated as multiplets corresponding to a given nl configuration and all possible values of the total angular momentum J. For instance, the x-ray diagram $L\alpha_{1,2}$ and $L\beta_1$ transitions investigated in the present work form the $2p^{-1} \rightarrow 3d^{-1}$ multiplet. If an additional vacancy is present in the atom during the transition, for example in the M-shell, three types of x-ray satellite lines appear in the spectrum which correspond to different locations of the additional vacancy, namely in the $3s$, $3p$, or $3d$ subshell. These satellite transitions belong to the multiplets $2p^{-1}3s^{-1} \to 3s^{-1}3d^{-1}$, $2p^{-1}3p^{-1} \to 3p^{-1}3d^{-1}$, or $2p^{-1}3d^{-1} \to 3d^{-2}$. If the additional vacancy is located in the L shell, i.e., in the $2s$ or $2p$ subshell, two x-ray hypersatellite transitions occur in the spectrum that corresponds to the multiplets $2p^{-1}2s^{-1} \to 2s^{-1}3d^{-1}$ and $2p^{-2} \to 2p^{-1}3d^{-1}$. As mentioned before, the number of possible x-ray transitions rapidly grows with the number of additional vacancies, in particular, for the outer shells. For example, for a configuration with four additional vacancies in the M shell corresponding to the $2p^{-1}3s^{-1}3p^{-2}3d^{-1} \to 3s^{-1}3p^{-2}3d^{-2}$ multiplet, the number of possible x-ray transitions in palladium is 94 008. If for the same element all possible configurations corresponding to four additional vacancies in the M shell are considered, the number of x-ray transitions grows to 244 953. Note that the total number of x-ray transitions computed for Pd with the MCDF method exceeded one million (1 171 157 exactly). An overview of the MCDF x-ray transitions calculated for Zr, Mo, and Pd is shown in Table I.

It should be mentioned also here that the complexity of the MCDF calculations depends strongly on the electronic configuration of the atom. For palladium, which has a closed-shell configuration ($[Kr]4d^{10}$), the MCDF calculations can be easily performed, even for high numbers of additional vacancies in the inner shells, because the number of transitions remains tractable. For zirconium ($[Kr]4d^{2}5s^{2}$) and molybdenum ($[Kr]4d^{5}5s^{1}$), however, which have open-shell configurations, the MCDF calculations are much more complicated. For example, for the diagram $L\alpha_{1,2}$ and $L\beta_1$ lines, only three transitions have to be calculated by the MCDF code for Pd, whereas for Zr (one open subshell) and Mo (two open subshells) the corresponding numbers of transitions are 1576 and 119 383, respectively. As a consequence, for Zr and Mo the use of the exact electron configurations makes the MCDF calculations practically impossible. To solve this problem, the following simplified electronic configurations were assumed for Zr and Mo: $[Kr]4d^4$ and $[Kr]5p^6$ which correspond to a configuration with a single open subshell and a configuration with all subshells closed, respectively. We would like to point out that the adopted configurations were found to give practically the same values for the average energies of the diagram transitions as the exact electronic configurations. Note also that the numbers of MCDF transitions presented in Table I for Zr and Mo were calculated using the simplified configurations.

The approximations discussed above in the MCDF calculations performed for free atoms evidence that possible solid-state effects can be neglected in interpretation of the measurements made on solids. First, the $L\alpha_{1,2}$ ($L_3\to M_{4,5}$) and $L\beta_1$ ($L_2\to M_4$) x-ray transitions in Zr, Mo, and Pd are core-to-core transitions involving L- and M-shell electrons for which the structure of valence-band $4d$ and $5s$ electrons is expected to play only a minor role. This was checked in fact using the MCDF calculations when the simplified closed subshell configurations were proposed to be used for open-shell zirconium ($[Kr]4d^{2}5s^{2}$) and molybdenum ($[Kr]4d^{5}5s^{1}$) atoms (see discussion above). Consequently, possible modifications of x-ray energies due to the $4d$ and $5s$ states being in the valence band in studied metals were neglected. One should also note that the solid-state effects can modify the decay rates, in particular, for the valence-band electrons [57]. However, since in the present paper the ionization probabilities only for the L and M shell were measured and discussed the solid-state effects can be neglected again.

V. X-RAY SPECTRA ANALYSIS

The measured $L\alpha_{1,2}$ and $L\beta_1$ x-ray spectra show complex structures due to the superposition of numerous diagram, satellite, and hypersatellite x-ray transitions corresponding to different multivacancy configurations. The pronounced features observed in these spectra (see Figs. 2–4), apart from the narrow diagram lines, are rather broad structures related to x-ray satellites ($L^{-1}M^{-m}N^{-n}$) and hypersatellites ($L^{-2}M^{-m}N^{-n}$). For each target the analysis of the x-ray spectrum was limited to the satellite and hypersatellite structures of the $L\alpha_{1,2}$ transition and the satellite structure of the $L\beta_1$ transition because the hypersatellite structure of the $L\beta_1$ transition was found to be affected by the contributions of the weak $L\beta_{2,15}$, $L\beta_3$, $L\beta_4$, and $L\beta_6$ lines as well as by the presence of the L_{III}-absorption edge.

To analyze the data, the calculated MCDF multiplets corresponding to the different multivacancy configurations (see Sec. IV) were fitted to the experimental x-ray spectra, taking into account the natural x-ray linewidths and instrumental broadening. The natural Lorentzian widths Γ_L of the x-ray transitions were determined by summing the total widths of the initial and final states, including in the case of multiply ionized atoms the contributions from the widths of the spectator vacancy states. In other words, the natural widths of the x-ray satellites or hypersatellites were calculated as follows:

$$\Gamma_L = \Gamma(i) + \Gamma(j) + 2\sum_k m_k \Gamma(k), \tag{9}$$

where $\Gamma(i)$ and $\Gamma(j)$ are the total widths of the initial i and final j states, m_k is the number of additional vacancies in the state k, and $\Gamma(k)$ is the natural width of this state. The natural widths of the single-hole states appearing in Eq. (9) were taken from the tables of Campbell and Papp [58]. The instrumental broadening was found to be well reproduced by a Gaussian profile having a width Γ_G of 0.3–0.6 eV, depending on the transition energy (see Sec. II A). Finally, to model the contributions of the multiplets corresponding to different multivacancy configurations on the experimental spectra, the sticklike distributions provided by the MCDF calculations were convoluted with the Lorentzian profiles of the corresponding x-ray transitions and the Gaussian function describing the instrumental broadening. As the convolution of a Lorentzian with a Gaussian results in a Voigtian function, the theoretically determined spectra consisted of many juxtaposed Voigtian profiles with centroids and areas equal to the energies and relative intensities provided by the MCDF calculations for the considered transitions. For illustration, the convoluted MCDF spectra corresponding to the dominant satellite and hypersatellite transitions in palladium are shown in Figs. 7 and 8, respectively.

According to the considerations presented above, the following function was employed to fit the experimental spectra:

$$S(E) = S_b(E) + \sum_i \alpha_i S_i^{\mathrm{MCDF}}(E), \tag{10}$$

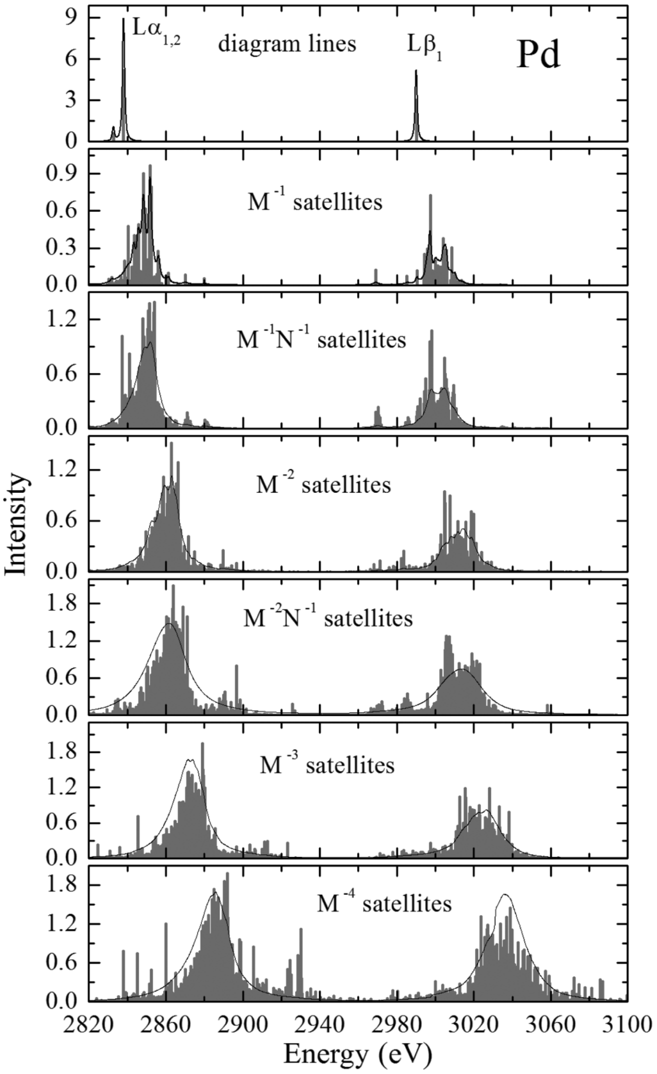

FIG. 7. MCDF stick spectra corresponding to the $L\alpha_{1,2}$ and $L\beta_1$ diagram and M- and N-shell satellite transitions of Pd. The height and position of a stick correspond to the relative intensity and energy of a particular MCDF transition. For the comparison with the experiment, Voigtian profiles with natural Lorentzian widths Γ_L and Gaussian instrumental broadenings Γ_G were attached to the sticks and summed up (black solid lines).

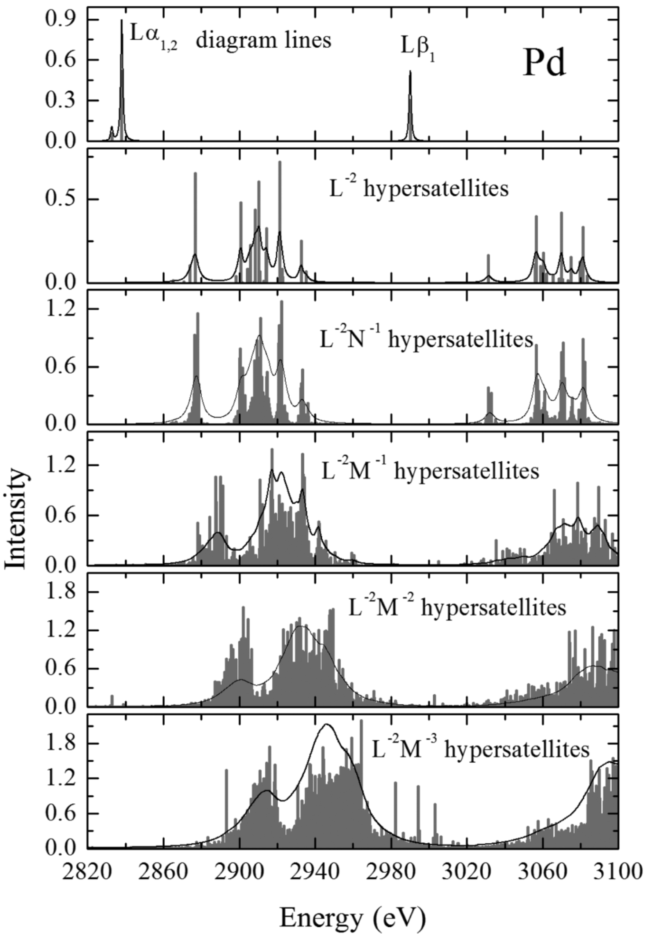

FIG. 8. Same as Fig. 7 but for the L-shell hypersatellite transitions of Pd.

where $S(E)$ represents the intensity of the measured spectrum, E is the x-ray energy, $S_b(E)$ is the background level, assumed to be described by the second-order polynomial, and $S_i^{\mathrm{MCDF}}(E)$ is the convoluted MCDF spectrum corresponding to the ith group of diagram, satellite, or hypersatellite transitions. The scaling factors α_i were used as free parameters in the fitting procedure. Due to the complexity of the free parameter optimization procedure the fitting was done in an iterative manner, which was found to be fast and unambiguous to interpret the measured x-ray spectra in terms of the MCDF calculations. In general, the vacancy configurations involving different l states could have been treated separately in the analysis. However, in order to speed up the fitting procedure the relative contributions of the s, p, and d states were weighted statistically, with the exception of some configurations involving p and d vacancy states that contributed to narrow spectral features due to their small Lorentzian widths.

The fits of the high-resolution $L\alpha_{1,2}$ and $L\beta_1$ x-ray spectra of Zr, Mo, and Pd induced by impact with oxygen ions are shown in Figs. 9–11. In these figures the MCDF-based interpretation of the measured x-ray structures in terms of x-ray satellites and hypersatellites is also depicted. The narrow lines appearing in the spectra correspond to the $L\alpha_{1,2}$ and $L\beta_1$ diagram lines, while the much wider structures occurring between the two diagram lines can be assigned, according to the MCDF predictions, to the M-shell satellites and L-shell hypersatellites. The diagram lines are substantially broadened due to the unresolved $L^{-1}N^{-n}$ satellites, which were calculated for $n \leqslant 2$. The M-shell satellite structures correspond to $L^{-1}M^{-m}N^{-n}$ transitions with up to $m = 4$ vacancies in the M shell and $n = 0,1$ vacancy in the N shell. Similarly, the hypersatellite structures corresponding to the $L^{-2}M^{-m}$ transitions were described by up to $m = 3$ vacancies in the M shell and zero or one vacancy in the N shell. A detailed description of the calculated MCDF configurations used to describe the measured spectra is given for the three target elements in Table I.

As shown in Figs. 9–11, the diagram $L\alpha_{1,2}$ and $L\beta_1$ lines are well separated from their $L^{-1}M^{-m}$ satellite structures in which components corresponding to $m \leqslant 3$ can be clearly

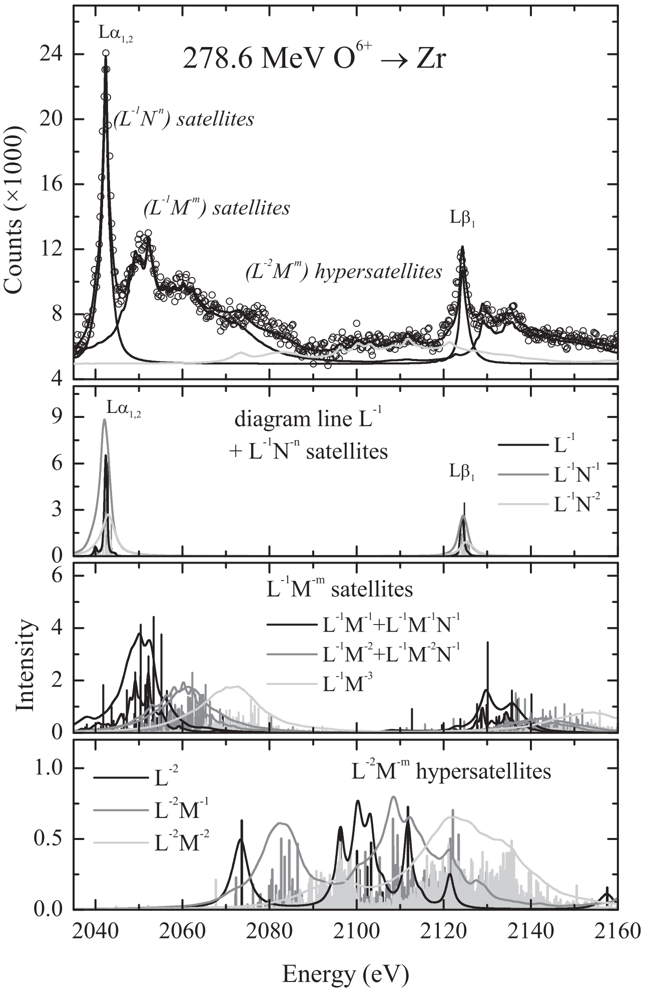

FIG. 9. Measured $L\alpha_{1,2} + L\beta_1$ x-ray spectrum of zirconium excited by 278.6-MeV oxygen ions (open circles in the top panel). The spectrum was fitted using the MCDF predicted profiles of the diagram lines and Nshell satellites (second panel from the top), M-shell satellites (third panel from the top) and L-shell hypersatellites (lowest panel).

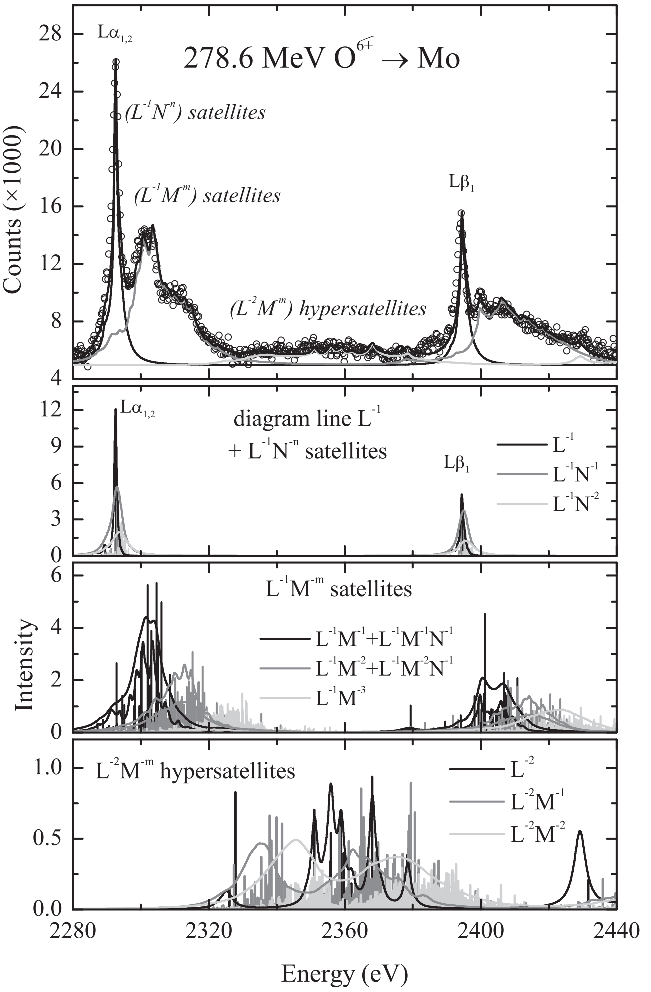

FIG. 10. Same as Fig. 9 but for molybdenum.

distinguished. The L-shell hypersatellites form a ∼100-eV-wide structure located between the M-shell satellites of the $L\alpha_{1,2}$ line and the $L\beta_1$ diagram line. As a consequence, the hypersatellites are the best visible for palladium because among the three investigated samples Pd is the one which has the largest separation energy between the $L\alpha_{1,2}$ and $L\beta_1$ lines. The N-shell satellites could not be resolved because for these satellites the energy shifts are smaller than the natural linewidths of the transitions. Thus, the unresolved N-shell satellites lead essentially to a broadening of the parent x-ray lines and to some asymmetry in their line shapes. For this reason $L^{-1,-2}M^{-m}N^{-n}$ configurations were included in the MCDF calculations whenever it was numerically tractable. In fact, due to the increasing complexity of the MCDF calculations for multivacancy configurations, in particular those involving outer shell vacancies, the calculations were limited to $m \leqslant 4$ vacancies in the M shell and up to $n = 1$ vacancy in the N shell (see Table I). However, even with this limitation the measured spectra of Zr, Mo, and Pd could be reproduced reasonably well by the MCDF calculations (see Figs. 9–11).

The fit quality of the measured spectra was quantified by probing the corresponding χ^2 values. For the three spectra, the χ^2/point values were found to be in the range 0.20–0.35. Furthermore, it should be noted that the employed MCDF-based method for the x-ray spectra analysis resulted in unambiguous and quite accurate estimations (±10–15%) of the scaling factors α_i of the individual MCDF structures [see Eq. (10)]. Actually, this was a crucial point for the interpretation of the experimental ionization probabilities in terms of theoretical predictions (see Sec. VII).

VI. EFFECTS OF MULTIPLE IONIZATION

The x-ray emission from atoms multiply ionized by ion impact is influenced by two main effects: (i) the vacancy rearrangement taking place between the moment of collision, i.e., the moment at which the atom is initially multiply ionized, and the later moment of x-ray emission and (ii) the modification of the atomic decay rates which change the x-ray fluorescence yields. As demonstrated below, the vacancy rearrangement processes, i.e., the time evolution of the vacancy distribution in multiply ionized atoms, can be described in terms of atomic decay rates for the radiative and radiationless Auger and

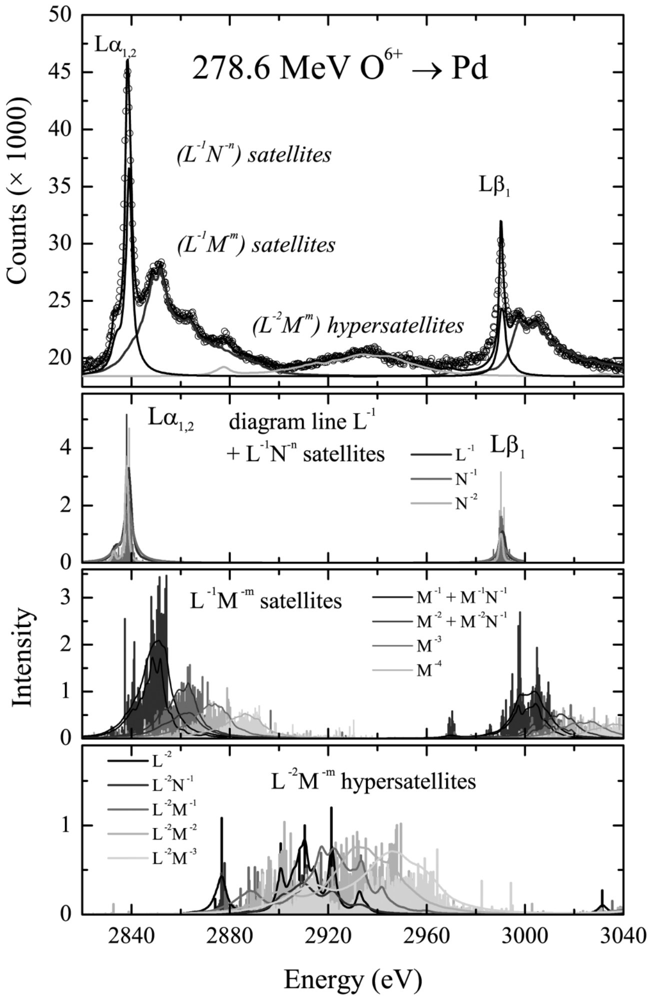

FIG. 11. Same as Fig. 9 but for palladium.

Coster-Kronig transitions, these transitions being themselves influenced by multivacancy states. As a consequence, in order to interpret correctly the measured x-ray spectra in terms of the collision-induced multiple ionization, the inner-shell vacancy rearrangement processes will be first discussed hereafter, following a method developed earlier [59,60].

A. Vacancy rearrangement processes

To understand the time evolution of the vacancy distribution prior to the x-ray emission, the following decay processes, which modify the distribution of vacancies, have to be considered: radiative transitions and radiationless Auger, Coster-Kronig (CK) and super-Coster-Kronig (sCK) transitions. Observing the flow of vacancies in multiply ionized atoms one finds that, in general, the vacancies are transferred to outer shells via one-electron radiative transitions and two-electron radiationless transitions. In the latter transitions which are autoionizing the number of initial vacancies is increased by 1. Furthermore, in an Auger transition the two final vacancies are located in outer shells with respect to the initial vacancy, in CK transitions one vacancy is located in the same shell as the primary vacancy and the second one in an outer shell, while in sCK transitions the two final vacancies are located in the same shell as the primary one.

The lifetime of a vacancy in the i subshell is inversely proportional to the total width Γ_i of this subshell. The total subshell width is given by the sum of the widths of all processes decaying a vacancy in this subshell, namely the radiative transitions (Γ_X) and the nonradiative Auger (Γ_A), Coster-Kronig ($\Gamma_{\rm CK}$), and super-Coster-Kronig ($\Gamma_{\rm sCK}$) transitions, as follows:

$$\Gamma_i = \Gamma_X + \Gamma_A + \Gamma_{\rm CK} + \Gamma_{\rm sCK}. \tag{11}$$

Taking into account the decay processes discussed above the change rate of the vacancy number for the i subshell can be expressed as

$$\frac{dn_i}{dt} = \sum_{k=1}^{i-1} (\Gamma_{k,i}/\hbar) n_k - (\Gamma_i/\hbar) n_i, \tag{12}$$

where Γ_i is the decay width of the i subshell, $\Gamma_{k,i}$ are the widths of the transitions transferring a vacancy from the k subshell into the i subshell, and n_i and n_k stand for the numbers of vacancies in subshells i and k at time t. As was shown in [60], Eq. (12) for a given shell represents a system of differential equations that can be solved analytically, starting from the first lowest subshell.

The number of vacancies $n_i(j)$ in the subshell i of the considered shell at the moment of the x-ray emission decaying a vacancy in the shell j can be calculated as the time-averaged number of vacancies $n_i(t)$ with respect to the lifetime of the state j [59,60]:

$$n_i(j) = \int_0^\infty n_i(t) \frac{\Gamma_j}{\hbar} e^{-\frac{\Gamma_j}{\hbar} t} dt, \tag{13}$$

where Γ_j is the natural width of shell j. By solving Eqs. (12) and (13) one obtains a general expression for the average number of vacancies in the i subshell [59]:

$$n_i(j) = \frac{\Gamma_j}{\Gamma_j + \Gamma_i} \left(n_i + \sum_{k=1}^{i-1} \frac{\Gamma_k}{\Gamma_j} f_{ki} n_k(j) \right), \tag{14}$$

where f_{ki} are the Coster-Kronig coefficients corresponding to the vacancy transitions from subshell k into subshell i. The calculation of the number of vacancies in any subshell was done iteratively, using Eq. (14) and starting from the lowest state $k = 1$. The values of the coefficients Γ_k and f_{ki} needed in the calculations were determined for the considered multivacancy configurations with the method described below (see Sec. VI B).

This procedure was used to calculate the average number of vacancies $n_i^m(j)$ in the subshell i at the moment of the x-ray emission decaying a vacancy in the subshell j for an assumed initial number n_i^m of vacancies, with m denoting the total number of vacancies in the shell containing the subshell i. Knowing the numbers $n_i^m(j)$ and n_i^m the correction factor $f_{\rm cor}(m)$, defined as the ratio of the number of vacancies at the moment of the x-ray emission to the number of initial vacancies in this shell, can be expressed as follows [59,60]:

$$f_{\rm cor}(m) = \frac{\sum_{i=1}^{k} n_i^m(j)}{\sum_{i=1}^{k} n_i^m}, \tag{15}$$

where $i = 1, \ldots, k$ denotes the different subshells of the considered shell. This way the number of vacancies at the moment of x-ray emission which is extracted from the relative intensities of the satellite or hypersatellite lines can be converted into the number of vacancies created by the collision, the latter number being the quantity that has to be compared to the predictions of the theoretical models describing the multiple ionization. It is worth noting here that the above correction factor $f_{\mathrm{cor}}(m)$ accounts for the multivacancy nature of the states for which the vacancy rearrangement is calculated.

B. Decay rates in multiply ionized atoms

Despite the fact that the decay rates of multiply ionized atoms depend on the multivacancy configuration, only values related to single-vacancy atoms are usually available in the literature (see Refs. [61–63]). This is due to the fact that calculations of radiative and, in particular, radiationless transition probabilities in multiply ionized atoms are very complicated and were performed only for a few specific cases (see Refs. [64–66]). For this reason such decay rates can only be estimated in an approximate way by taking into account only the dominating effects among those leading to a change of the decay rates between singly and multiply ionized atoms. Generally, there are two main effects influencing the decay rates which can be treated within simplified approaches, namely, (i) the reduction of the number of available electrons [67] and (ii) the closing of particular Coster-Kronig decay channels in multiply ionized atoms. Both of these effects change the partial decay widths Γ_X of the radiative transitions, respectively Γ_A, Γ_{CK}, and Γ_{sCK} of the radiationless ones.

The first effect related to the reduced number of available electrons in multiply ionized atoms can be treated by the statistical scaling method proposed by Larkins [67]. This method assumes that single-vacancy decay widths are reduced by a factor reflecting the relative decrease of the number of available electrons for a given transition.

The second effect, which can influence substantially the decay rates, is the closing of certain Coster-Kronig transitions in multiply ionized atoms. This effect can be accounted for by calculating the energies of the electrons emitted in Coster-Kronig transitions, which have to be positive for allowed CK channels. Using the approach which was proposed in our earlier paper [59], the electron energy $\varepsilon_{\mathrm{diag}}$ for the diagram Coster-Kronig transition i-jk can be approximated as follows:

$$\varepsilon_{\mathrm{diag}}^{i-jk} = B_i(Z) - B_j(Z) - B_k(Z+1), \tag{16}$$

where $B_s(Z)$ is the binding energy of a s-shell electron for the element with the atomic number Z. Using the approximation known as the "$Z+1$" rule the modification of the electron binding energy δB_s due to the creation of one additional vacancy in the s shell is given by

$$\delta B_s = B_s(Z+1) - B_s(Z+2). \tag{17}$$

Consequently, the Coster-Kronig transition energy $\varepsilon^{i-jk}(m,n)$ in the presence of m vacancies in the M shell and n vacancies in the N shell can be expressed as follows:

$$\varepsilon^{i-jk}(m,n) = \varepsilon_{\mathrm{diag}}^{i-jk} + m\delta B_m + n\delta B_n, \tag{18}$$

where δB_m and δB_n are given by Eq. (17).

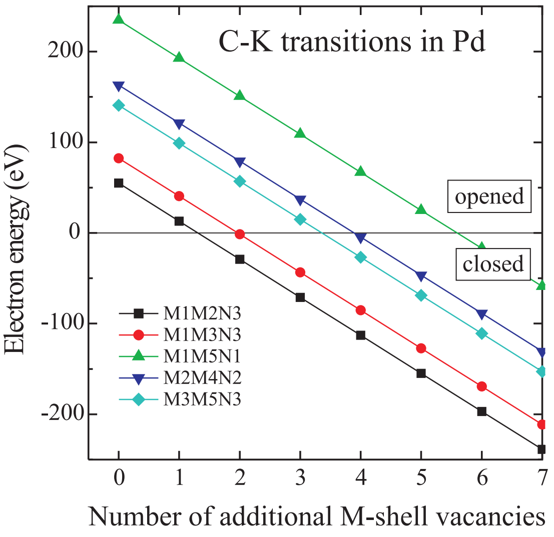

FIG. 12. (Color online) Energies of selected Coster-Kronig transitions in palladium as a function of the number of spectator vacancies in the M shell.

Due to the increase of the vacancy number, the energy of the Coster-Kronig transition decreases and when the latter becomes lower than zero, the Coster-Kronig transition is energetically forbidden. This effect is demonstrated in Fig. 12 for selected Coster-Kronig transitions in palladium. As a result of the closing of one or more Coster-Kronig transitions the total CK width is modified, which in turn influences the CK rates f_{ki} and fluorescence yields ω_i as well as the value of the correction factor $f_{\mathrm{cor}}(m)$ introduced in Eq. (15). The modified M-shell Coster-Kronig yields f_{ki} and L-shell fluorescence yields ω_i in palladium are shown in Figs. 13 and 14, respectively. Similarly, the calculated dependence of the correction factor $f_{\mathrm{cor}}(m)$ on

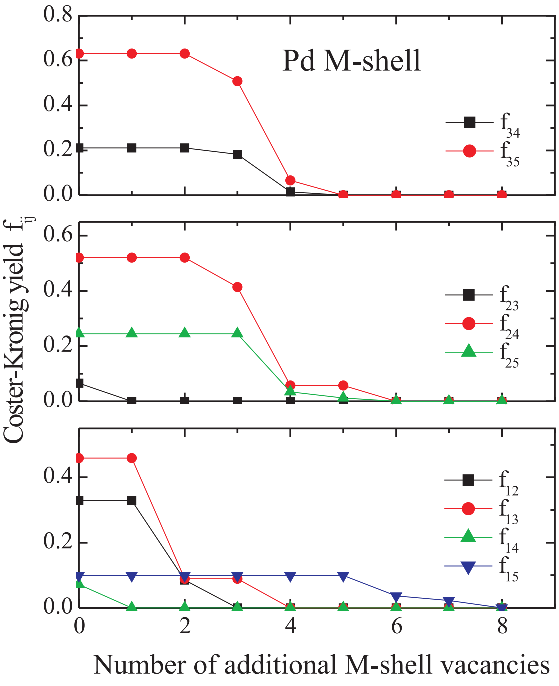

FIG. 13. (Color online) Coster-Kronig yields f_{ki} for the M shell of palladium as a function of the number of spectator vacancies in the M shell.

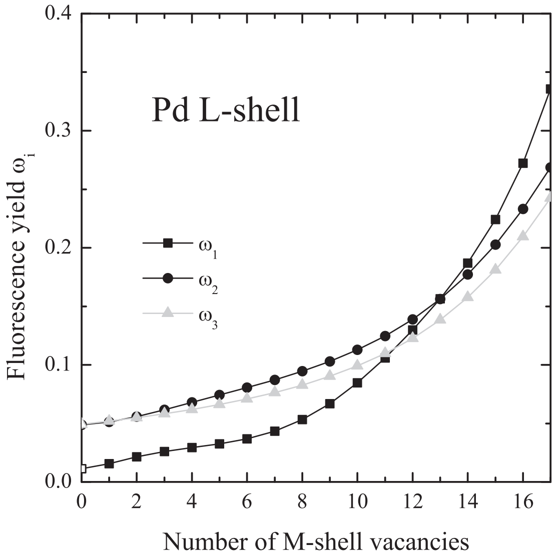

FIG. 14. L-shell fluorescence yields ω_i of palladium as a function of the number of M-shell vacancies.

the number of vacancies in the M shell is shown in Fig. 15 for the satellite and hypersatellite transitions in Pd.

Finally, knowing the correction factor $f_{\mathrm{cor}}(m)$ for the vacancy rearrangement and the modified fluorescence yield $\omega_i(m)$ for the L_i subshells, the distribution $I_{\mathrm{obs}}(m)$ of the *observed* satellite or hypersatellite intensities can be related to the distribution $P(m)$ of the vacancies formed at the moment of the collision as follows:

$$I_{\mathrm{obs}}(m) \propto P(m) f_{\mathrm{cor}}(m) \omega_i(m), \tag{19}$$

where m represents the number of vacancies at the moment of the collision. This relation was used to derive the initial distributions of vacancies $P(m)$ from the observed satellite and hypersatellite intensity distributions $I_{\mathrm{obs}}(m)$.

As shown for palladium in Figs. 14 and 15 the effects changing the fluorescence yields and vacancy rearrangement in multiply ionized ions influence the x-ray intensities in the opposite way, one effect partly compensating the other one. Actually the L-shell fluorescence yields grow systematically with the number of additional vacancies, the relative increase being about 20% for four vacancies in the M shell. On the other hand, the vacancy rearrangement generally decreases the intensities of the x rays up to 8% for satellites and up to 5% for hypersatellites. Note that the partial compensation of the two effects results in rather small corrections for the observed x-ray intensities [see Eq. (19)] and consequently for the initial vacancy distributions $P(m)$. In fact, the net correction was about 10% for palladium and slightly smaller for zirconium and molybdenum.

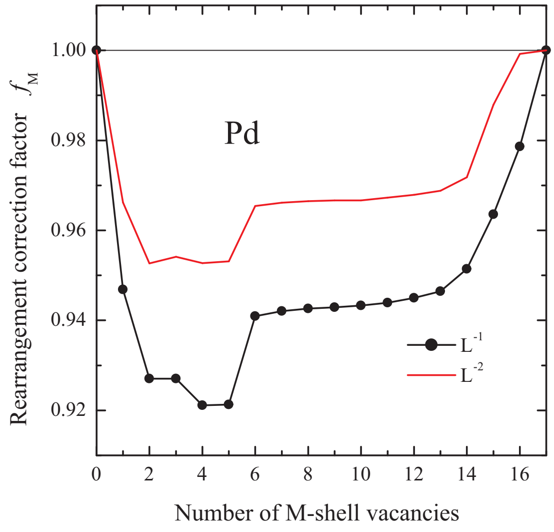

FIG. 15. (Color online) Correction factor $f_{\mathrm{cor}}(m)$ [Eq. (15)] for palladium as a function of the number of M-shell vacancies.

VII. IONIZATION PROBABILITIES

The measured intensities of the x-ray satellites and hypersatellites of the $L\alpha_{1,2}$ ($L_3 \rightarrow M_{4,5}$) transitions in zirconium, molybdenum, and palladium were used to determine the ionization probabilities for the L and M shell at the moment corresponding to the impact of the fast oxygen ions. This was done by comparing the relative intensities of the diagram, satellite, and hypersatellite x-ray lines with the predictions of the independent particle model, assuming the latter to be applicable for the description of the multiple ionization induced by the investigated collisions. More precisely, the L-shell ionization probabilities were deduced from the relative intensities of the $L^h\alpha_{1,2}$ x-ray hypersatellites by comparing the measured intensity ratios

$$R = I(L^h\alpha_{1,2})/[I(L\alpha_{1,2}) + I(L^{\mathrm{sat}}\alpha_{1,2})] \tag{20}$$

with the corresponding theoretical predictions. Similarly, the M-shell ionization probabilities were determined by fitting the measured intensity distributions of the $L^{\mathrm{sat}}\alpha_{1,2}(M^{-m})$ satellites with binomial distributions. The intensities of the x-ray diagram, satellite, and hypersatellite lines needed for this purpose were obtained by fitting the calculated MCDF structures corresponding to the multivacancy configurations $L^{-1,-2}M^{-m}N^{-n}$ to the measured x-ray spectra (see Sec. V). The total intensities of the $L\alpha_{1,2}$, $L^{\mathrm{sat}}\alpha_{1,2}(M^{-m})$, and $L^h\alpha_{1,2}$ lines were calculated by summing the intensities of the fitted x-ray transitions corresponding to the $L^{-1,-2}M^{-m}N^{-n}$ configurations. This procedure permitted us to probe the goodness of the independent particle model as well as to determine the L- and M-shell ionization probabilities per electron $p_L(0)$ and $p_M(0)$ for central collisions.

The measured ionization probabilities can be interpreted in terms of the independent particle model and the impact parameter formulation of the semiclassical approximation. Within this approach the probability for the creation by impact with heavy ions of a given multivacancy configuration $L^{-1,-2}M^{-m}N^{-n}$ is described by a binomial probability [see Eq. (2)] parametrized by the impact parameter dependent ionization probability per electron $p(b)$. As shown in Figs. 5 and 6, the probabilities $p(b)$ can be assumed to be nearly independent from the subshell, i.e., a single average ionization probability can be used for the L or M shell. This simplifying approximation was necessary for the application of the adopted method. Note that the impact parameter dependent ionization probabilities $p(b)$ can be calculated within the semiclassical approximation discussed in Sec. III C.

The emission of the $L\alpha_{1,2}$ ($L_3 \rightarrow M_{4,5}$) diagram x-ray transition results from the radiative decay of a single vacancy in the L_3 subshell. In multiply ionized atoms this transition forms a complex spectrum consisting of diagram, satellite, and hypersatellite lines corresponding to different multivacancy configurations $L^{-1,-2}M^{-m}N^{-n}$, whose relative intensities can be described theoretically as discussed above. Consequently, the intensity ratio of the $L\alpha_{1,2}$ hypersatellite to summed diagram and M-satellite transitions defined in Eq. (20) can be rewritten as

$$R = \frac{\left[\binom{4}{1}\binom{4}{1} + \binom{4}{2}\right] \int_0^{\infty} b[p_L(b)]^2[1 - p_L(b)]^6 db}{\binom{4}{1} \int_0^{\infty} b p_L(b)[1 - p_L(b)]^7 db}, \qquad (21)$$

where the factorials are the statistical weights corresponding to the binomial distribution of the spectator vacancies with the constraint that for the diagram or M-satellite transition the single L-shell vacancy should be located in the L_3 subshell, whereas for the hypersatellite transition at least one vacancy has to be located in the L_3 subshell and another one in any other L subshell. As shown by Eq. (21), the ratio R is determined by integrating the ionization probability $p_L(b)$ over a wide range of the impact parameter and consequently the zero impact ionization probability $p_L(0)$ cannot be extracted directly from the R value. However, writing $p_L(b) = p_L(0)\chi_L(b)$ and assuming that the function $\chi_L(b)$ can be determined theoretically using, e.g., the SCA model, the ionization probabilities $p_L(0)$ can be derived from the experimental data. In this approach $p_L(0)$ is treated as a scaling parameter to be determined from the comparison of the theoretical [see Eq. (21)] and experimental [see Eq. (20)] values of the ratio R. In fact, this is demonstrated in Fig. 16 where the dependence of the ratio R is plotted as a function of $p_L(0)$ using theoretical predictions for $p_L(b)$. The probabilities $p_L(b)$ were calculated with the SCA approximation using relativistic hydrogenic wave functions (SCA-HYD) and self-consistent Dirac-Hartree-Fock wave functions (SCA-DHF).

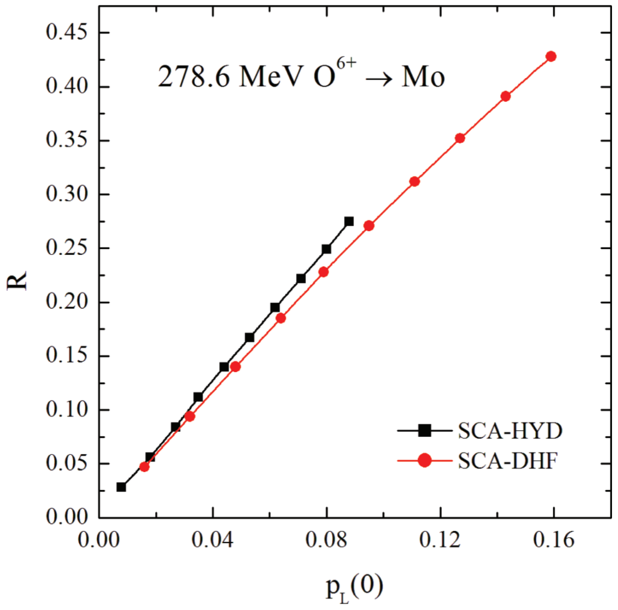

FIG. 16. (Color online) Dependence of the hypersatellite to diagram plus satellite intensity ratio R [Eq. (21)] on the ionization probability per electron for central collisions $p_L(0)$ as calculated within the SCA-HYD and SCA-DHF approaches.

TABLE II. Experimental and theoretical values of the hypersatellite to diagram plus M-satellite intensity ratios R for the three investigated collisions. Also listed are the experimental and theoretical L-shell ionization probabilities $p_L(0)$. The experimental values were deduced from the corresponding ratios R and the theoretical ones from calculations using the SCA approximation and the geometrical model.

	Element		
	Zr	Mo	Pd
	R ratio		
Experiment	0.266 ± 0.026	0.233 ± 0.035	0.214 ± 0.031
SCA(HYD)	0.254	0.140	0.101
SCA(DHF)	0.226	0.228	0.164
	Ionization probability $p_L(0)$		
Experiment	0.088 ± 0.010	0.081 ± 0.013	0.102 ± 0.016
GM	0.105	0.103	0.098
SCA(HYD)	0.044	0.044	0.044
SCA(DHF)	0.081	0.078	0.076

The observed and calculated L-shell ionization probabilities for zirconium, molybdenum, and palladium were compared in two ways. First, the measured [Eq. (20)] and calculated [Eq. (21)] values of the R ratios were directly compared using the theoretical predictions of the SCA-HYD and SCA-DHF models. Second, using the SCA-DHF calculations which provide for the ratio R values which are, except for Zr, closer to the experimental ones, the L-shell ionization probabilities for central collisions $p_L(0)$ were determined by solving the equation $R[p_L(0)] = R_{\text{exp}}$ (see Fig. 16). The measured and calculated values of the ratio R and the deduced ionization probabilities $p_L(0)$ are presented for the three target elements in Table II. The corresponding theoretical predictions of the SCA model using relativistic hydrogenic (SCA-HYD) and self-consistent (SCA-DHF) wave functions are also reported in Table II as well as the ionization probabilities $p_L(0)$ calculated according to the geometrical model (GM) [37].

The experimental ratios R obtained for Zr, Mo, and Pd (see Table II) slightly decrease with the atomic number of the studied elements, being in the range 0.266–0.214 (±15%). They agree within 10% with the predictions of the SCA-HYD and SCA-DHF calculations for Zr and Mo. For Pd the SCA-HYD prediction is a factor of 2 smaller than the measured value. In this case the use of the more realistic SCA-DHF calculations yields for R a value of 0.164 which is closer to the experimental result (0.214), indicating that the relativistic self-consistent DHF wave functions are more reliable to reproduce the studied R ratios. For this reason the SCA-DHF wave functions were used to extract the ionization probabilities $p_L(0)$ for central collisions as mentioned earlier (see Fig. 16). For the investigated 4d transition elements the experimental probabilities are in the range 0.088–0.102 (±15%). In this case the SCA-HYD predictions are systematically smaller by a factor of 2, while the SCA-DHF are in reasonable agreement with the data (±8–20%). One also observes here that the nonrelativistic geometrical model (GM) provides probabilities which are, somewhat surprisingly, in quite satisfactory agreement with the experimental values.

For the M shell the ionization probabilities $p_M(0)$ corresponding to central collisions were obtained from the measured intensities of the M-shell satellites of the $L\alpha_{1,2}$ $[L_3 \rightarrow M_{4,5}(M^{-m})]$ x-ray transition. In this case the typical impact parameter values contributing to the creation of a vacancy in the L_3 subshell are much smaller than those corresponding to the ionization of the M shell. As a consequence the probability for the creation of $L_3^{-1}M^{-m}$ configurations corresponding to the M-shell satellites can be approximated by $p_M(0)$. However, in order to extract the experimental ionization probabilities from the intensities of the measured M-shell satellites, the latter have to be corrected beforehand for the vacancy rearrangement processes and change of fluorescence yields as discussed in Sec. VI A. Finally, the probability for the creation of m vacancies in the M shell can be described by the following binomial distribution:

$$P_M(m) = \binom{17}{m}[p_M(0)]^m[1 - p_M(0)]^{17-m}, \qquad (22)$$

where $p_M(0)$ is the ionization probability per electron at the moment of the collision for an impact parameter equal to 0. Here the vacancies can be created only out of $N_M = 17$ electrons in the M shell since one electron has to be involved in the observed $L\alpha_{1,2}(L_3 \rightarrow M_{4,5})$ x-ray transition.

For illustration, the distributions of the measured and corrected intensities of the M-shell satellites are shown for zirconium, molybdenum, and palladium in Figs. 17–19. The corrected intensities were determined from Eq. (19). They correspond to the M-shell vacancy distribution at the moment of the collision. The latter distribution was fitted using the binomial distribution given in Eq. (22) to extract the ionization probability $p_M(0)$. The obtained M-shell ionization probabilities are listed in Table III together with the corresponding theoretical predictions provided by the SCA-HYD, SCA-DHF, and GM models. The values of the experimental ionization probabilities $p_M(0)$ of the three target elements are in the range 0.079–0.062 (±8–12%). They were found to agree with the predictions of the SCA-DHF calculations within 5–20%. As for the L shell the SCA-HYD calculations predict values that are systematically smaller than the measured ones, the discrepancies being, however, much higher for the M shell (almost a factor 4). This indicates that the use of realistic wave functions in the SCA model is mandatory for the M shell. Regarding the geometrical model (GM), ionization probabilities $p_M(0) \simeq 0.055$ are found which are systematically smaller (±8–20%) than the experimental values but not as much as those predicted by the SCA-HYD calculations.

Generally, the ionization probabilities for central collisions $p_L(0)$ and $p_M(0)$ extracted from the data agree within about

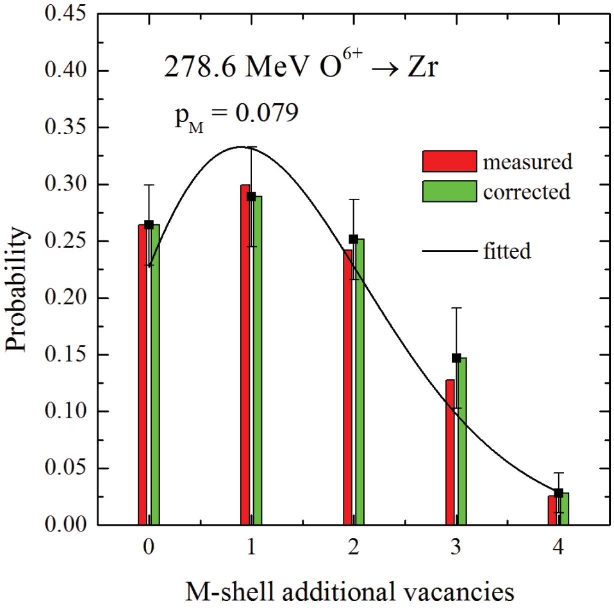

FIG. 17. (Color online) Measured and corrected intensities of the M-shell satellites of zirconium excited by 278.6-MeV oxygen ions. The curve corresponds to a binomial distribution with a fitted value $p_M = 0.079$ for the M-shell ionization probability.

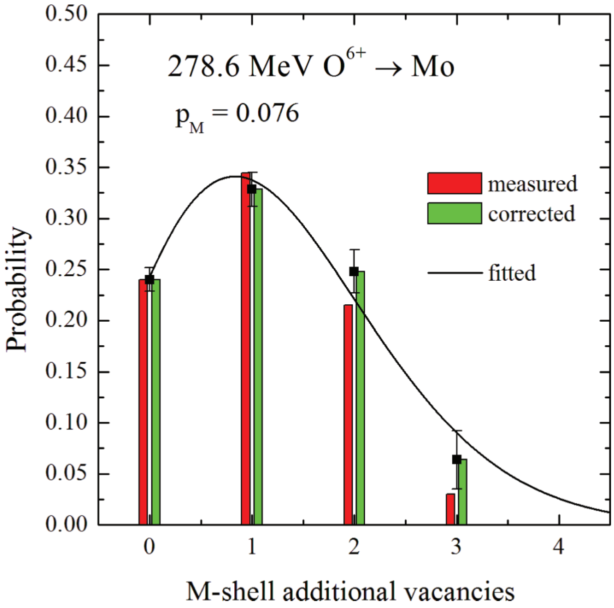

FIG. 18. (Color online) Same as Fig. 17 but for molybdenum.

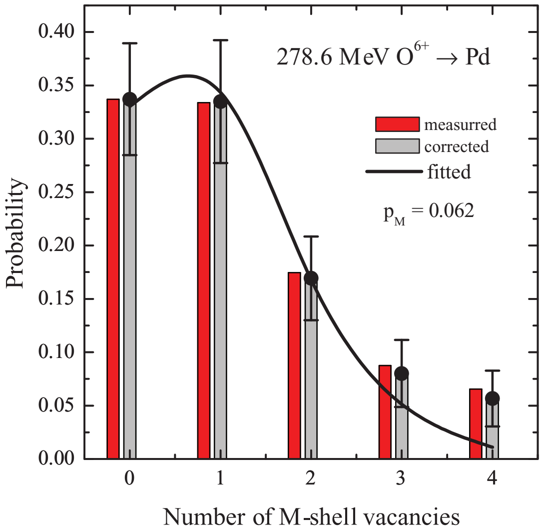

FIG. 19. (Color online) . Same as Fig. 17 but for palladium.

TABLE III. Experimental values of the ionization probabilities $p_M(0)$ obtained from the measured and corrected experimental spectra. Theoretical values were calculated using the SCA and geometrical models.

	Element		
	Zr	Mo	Pd
	Ionization probability $p_M(0)$		
Experiment	0.079 ± 0.006	0.076 ± 0.005	0.062 ± 0.007
GM	0.056	0.056	0.055
SCA(HYD)	0.022	0.022	0.022
SCA(DHF)	0.074	0.075	0.076

20% with the predictions of the semiclassical approximation using self-consistent relativistic Dirac-Hartree-Fock wave functions (SCA-DHF). This level of agreement seems to be acceptable with respect to the experimental uncertainties (15%) of the measured ionization probabilities and necessary approximations that should be done to interpret the data.

VIII. SUMMARY AND CONCLUSIONS

$L\alpha_{1,2}$ and $L\beta_1$ satellite and hypersatellite x-ray spectra of $_{40}$Zr, $_{42}$Mo and $_{46}$Pd were measured by means of high-resolution x-ray spectroscopy using a Bragg-type von Hamos bent crystal spectrometer. The target fluorescence was produced by bombarding the samples with fast oxygen ions. As the measured satellite and hypersatellite structures reflect the multivacancy configurations of the target atoms at the moment of the x-ray emission, the multiple ionization at the impact time was determined by taking into account all inner-shell vacancy rearrangement processes that take place prior to the x-ray emission. The intensities of the measured x-ray satellites and hypersatellites reflect thus the structure and the relaxation processes of multiply ionized atoms. Regarding the relaxation processes, it was shown that the influence of the multiple ionization on the radiative and radiationless decay rates has to be considered, in particular the effects related to the closure of certain Coster-Kronig transitions.

The measured x-ray spectra were interpreted with the help of MCDF calculations with which the structures of the x-ray satellites and hypersatellites corresponding to individual multivacancy $L^{-1,-2}M^{-m}N^{-n}$ configurations could be predicted. $L\alpha_{1,2}$ satellites and hypersatellites and $L\beta_1$ satellites with up to four additional vacancies in the M and N shells were considered in the calculations. In the MCDF approach the number of calculated x-ray transitions depends strongly on the electronic structure of the investigated atom. For instance, for palladium which has all its subshells closed, more than one million x-ray transitions were computed. For zirconium and molybdenum which are characterized by one or two open subshells in the ground state, the numbers of x-ray transitions to be calculated were even much higher and therefore the calculations were no more tractable. For this reason, simplified ground-state configurations had to be adopted for these elements corresponding to configurations with a single open subshell (Zr) or all subshells closed (Mo). As a consequence, the numbers of calculated MCDF x-ray transitions were in general smaller for Zr and Mo than for Pd.

It was found that, in general, the measured x-ray spectra could be well reproduced by the MCDF calculations. This allowed us to analyze the spectra in a reliable way. From the fits of the MCDF spectra to the experimental ones, the intensities of the satellite and hypersatellite x-ray transitions could be determined. After correction of these intensities to account for the rearrangement processes, the probabilities for the L and M-shell ionization of Zr, Mo, and Pd by 278.6-MeV oxygen ions in nearly central collisions could be determined. More precisely, the L-shell ionization probabilities $p_L(0)$ were deduced from the $L\alpha_{1,2}$ hypersatellites to diagram + M-satellite intensity ratios, while the M-shell ionization probabilities $p_M(0)$ were determined by fitting the corrected relative intensities of the M-shell satellites to a binomial distribution, using the probabilities $p_M(0)$ as free fitting parameters.

The obtained ionization probabilities $p_L(0)$ and $p_M(0)$ were compared with predictions of existing theoretical models, namely the geometrical model (GM) based on the binary encounter approximation (BEA) and the semiclassical approximation (SCA). In the GM calculations nonrelativistic hydrogenic wave functions were used, while in the SCA approach Dirac hydrogenic wave functions (SCA-HYD) and more realistic Dirac-Hartree-Fock selfconsistent wave functions (SCA-DHF) were employed. Here it should be noted that the calculations concerning the relative hypersatellite intensities, i.e., the R ratios, could be performed only within the SCA approximation, because the geometrical model does not provide the dependence of the ionization probability on the impact parameter which is needed for the calculation of the ratios R [see Eq. (21)].

The experimental results for the ratios R used to study the multiple ionization in the L shell were found to be systematically higher than the SCA-DHF values (up to about 20%), while the SCA-HYD predictions were found to be more than two times smaller. Similar trends were found for the ionization probabilities $p_L(0)$. This is, however, not surprising since the latter were derived from the measured ratios R. The experimental M-shell ionization probabilities $p_M(0)$ agree with the theoretical SCA-DHF values within the experimental uncertainties for zirconium and molybdenum, whereas for palladium the experimental value is smaller by about 20%. As for the L shell the predictions of the SCA-HYD approximation are systematically smaller than the experimental values, but in this case by a factor of about 3. This indicates that a realistic description of the electronic wave functions such as the one provided by the relativistic self-consistent Dirac-Hartree-Fock approach is required to get reliable ionization probabilities, especially in the case of outer shells. To summarize, the present paper has demonstrated that the interpretation of x-ray spectra from multiply ionized atoms needs both relativistic MCDF calculations to describe the structure of the measured x-rays and relativistic Dirac-Hartree-Fock wave functions in the SCA-DHF calculations to describe the multivacancy configurations contributing to the x-ray emission.

Finally, we would like to point out that the developed calculations of the x-ray emission from multiply ionized atoms are of great importance for modeling the complex x-ray spectra emitted by astrophysical and laboratory plasma as well as by exotic hollow atoms which are created by the interaction of highly charged ions (HCIs) with surfaces and the irradiation of matter with intense XFEL x-ray beams. For these reasons, it can be expected that the multiple ionization processes discussed in this paper will be intensively studied in the near future.

ACKNOWLEDGMENTS

The authors would like to thank Dr. P. Schmelzbach and his collaborators from the PSI for providing our experiment with very good beam conditions at the Philips cyclotron. The financial support of the Swiss National Science Foundation and the Polish National Science Centre under Grant No. 2011/01/D/ST2/01286 is acknowledged.

[1] M. Siegbahn and W. Stenström, Phys. Z. **17**, 48 (1916).

[2] J. P. Briand, P. Chevallier, M. Tavernier, and J. P. Rozet, Phys. Rev. Lett. **27**, 777 (1971).

[3] C. J. Burbank, Phys. Rev. **56**, 142 (1939).

[4] R. D. Richtmyer, Phys. Rev. **56**, 146 (1939).

[5] F. R. Hirsh, Rev. Mod. Phys. **14**, 45 (1942).

[6] G. Charpak, C. R. Acad. Sci. T **237**, 243 (1953).

[7] J. P. Briand, P. Chevallier, and M. Tavernier, J. Phys. Colloq. **32**, C4-165 (1971).

[8] A. Migdal, J. Phys. (Moscow) **4**, 449 (1941).

[9] E. L. Feinberg, J. Phys. (Moscow) **4**, 423 (1941).

[10] R. Diamant, S. Huotari, K. Hämäläinen, R. Sharon, C. C. Kao, and M. Deutsch, Phys. Rev. A **79**, 062511 (2009).

[11] J. Hoszowska, A. K. Kheifets, J.-Cl. Dousse, M. Berset, I. Bray, W. Cao, K. Fennane, Y. Kayser, M. Kavčič, J. Szlachetko *et al.*, Phys. Rev. Lett. **102**, 073006 (2009).

[12] P. Auger, J. Phys. Radium **6**, 205 (1925).

[13] D. Coster and R. de L. Kronig, Physica **2**, 13 (1935).

[14] P. Richard, *Atomic Inner-Shell Processes* (Academic, New York, 1975), p. 73.

[15] P. Richard, W. Hodge, and C. F. More, Phys. Rev. Lett. **29**, 393 (1972).

[16] M. H. Chen, B. Crasemann, and H. Mark, Phys. Rev. A **25**, 391 (1982).

[17] D. K. Olsen and C. F. More, Phys. Rev. Lett. **33**, 194 (1974).

[18] B. Boschung, J.-Cl. Dousse, B. Galley, Ch. Herren, J. Hoszowska, J. Kern, Ch. Rhême, Z. Halabuka, T. Ludziejewski, P. Rymuza *et al.*, Phys. Rev. A **51**, 3650 (1995).

[19] J. Rzadkiewicz, D. Chmielewska, T. Ludziejewski, P. Rymuza, Z. Sujkowski, D. Castella, D. Corminboeuf, J.-Cl. Dousse, B. Galley, Ch. Herren *et al.*, Phys. Lett. A **264**, 186 (1999).

[20] M. Czarnota, D. Banaś, M. Berset, D. Chmielewska, J.-Cl. Dousse, J. Hoszowska, Y.-P. Maillard, O. Mauron, M. Pajek, M. Polasik *et al.*, Phys. Rev. A **81**, 064702 (2010).

[21] M. Czarnota, D. Banaś, M. Berset, D. Chmielewska, J.-Cl. Dousse, J. Hoszowska, Y.-P. Maillard, O. Mauron, M. Pajek, M. Polasik *et al.*, Eur. Phys. J. D **57**, 321 (2010).

[22] S. M. Kahn, M. A. Leutenegger, J. Cottam, G. Rauw, J.-M. Vreux, A. J. F. den Boggende, R. Mewe, and M. Güdel, Astron. Astrophys. **365**, L312 (2001).

[23] C. A. Back, J. Grun, C. Decker, L. J. Suter, J. Davis, O. L. Landen, R. Wallace, W. W. Hsing, J. M. Laming, and U. Feldman, Phys. Rev. Lett. **87**, 275003 (2001).

[24] J. Dunn, A. L. Osterheld, R. Shepherd, W. E. White, V. N. Shlyaptsev, and R. E. Stewart, Phys. Rev. Lett. **80**, 2825 (1998).

[25] L. Young, E. P. Kanter, B. Krässig, Y. Li, A. M. March, S. T. Pratt, R. Santra, S. H. Southworth, N. Rohringer, L. F. DiMauro *et al.*, Nature (London) **466**, 56 (2010).

[26] J. P. Briand, L. de Billy, P. Charles, S. Essabaa, P. Briand, R. Geller, J. P. Desclaux, S. Bliman, and C. Ristori, Phys. Rev. Lett. **65**, 159 (1990).

[27] Z. Hu, X. Han, Y. Li, D. Kato, X. Tong, and N. Nakamura, Phys. Rev. Lett. **108**, 073002 (2012).

[28] S. M. Vinko, O. Ciricosta, B. I. Cho, K. Engelhorn, H.-K. Chung, C. R. D. Brown, T. Burian, J. Chalupský, R. W. Falcone, C. Graves, V. Hájková *et al.*, Nature (London) **482**, 59 (2012).

[29] T. R. Johnson and K. T. Chang, *Atomic Inner-Shell Physics* (Plenum, New York, 1985), pp. 3–30.

[30] I. P. Grant, B. J. McKenzie, P. H. Norrington, D. F. Mayers, and N. C. Pyper, Comput. Phys. Commun. **21**, 207 (1980).

[31] M. Polasik, Phys. Rev. A **39**, 616 (1989).

[32] G. Breit, Phys. Rev. **39**, 616 (1932).

[33] J. B. Mann and W. R. Johnson, Phys. Rev. A **4**, 41 (1971).

[34] J. Hoszowska, J.-Cl. Dousse, J. Kern, and C. Rhême, Nucl. Instrum. Methods Phys. Res. A **376**, 129 (1996).

[35] R. D. Deslattes, J. E. G. Kessler, P. Indelicato, L. de Billy, E. Lindroth, and J. Anton, Rev. Mod. Phys. **75**, 35 (2003).

[36] J. H. McGuire and P. Richard, Phys. Rev. A **8**, 1374 (1973).

[37] B. Sulik, I. Kádár, S. Ricz, D. Varga, J. Végh, G. Hock, and D. Berényi, Nucl. Instrum. Methods Phys. Res. B **28**, 509 (1987).

[38] D. Trautmann and F. Rösel, Nucl. Instrum. Methods **169**, 259 (1980).

[39] D. Trautmann and T. Kauer, Nucl. Instrum. Methods Phys. Res. B **42**, 449 (1989).

[40] J. H. McGuire and L. Weaver, Phys. Rev. A **16**, 41 (1977).

[41] B. Sulik, G. Hock, and D. Berényi, J. Phys. B **17**, 3239 (1984).

[42] M. Gryziński, Phys. Rev. **138**, A305 (1965); **138**, A322 (1965); **138**, A336 (1965).

[43] D. Trautmann, F. Rösel, and G. Baur, Nucl. Instrum. Methods Phys. Res. **214**, 21 (1983).

[44] D. Trautmann and G. Baur, Nucl. Instrum. Methods Phys. Res. B **40-41**, 345 (1989).

[45] W. F. Perger, Z. Halabuka, and D. Trautmann, Comput. Phys. Commun. **76**, 250 (1993).

[46] Z. Halabuka, W. Perger, and D. Trautmann, Z. Phys. D **29**, 151 (1994).

[47] M. Polasik, Phys. Rev. A **39**, 5092 (1989).

[48] M. Polasik, Phys. Rev. A **41**, 3689 (1990).

[49] M. Polasik, Phys. Rev. A **52**, 227 (1995).

[50] M. W. Carlen, M. Polasik, B. Boschung, J.-Cl. Dousse, M. Gasser, Z. Halabuka, J. Hoszowska, J. Kern, B. Perny, C. Rhême *et al.*, Phys. Rev. A **46**, 3893 (1992).

[51] B. J. McKenzie, I. P. Grant, and P. H. Norrigton, Comput. Phys. Commun. **21**, 233 (1980).

[52] I. P. Grant, Int. J. Quatum Chem. Phys. **25**, 23 (1984).

[53] K. G. Dyall, I. P. Grant, C. T. Johnson, F. A. Parpia, and E. P. Plummer, Comput. Phys. Commun. **55**, 425 (1989).

[54] F. A. Parpia, C. F. Fisher, and I. P. Grant, Comput. Phys. Commun. **94**, 249 (1996).

[55] I. P. Grant, J. Phys. B **7**, 1458 (1974).

[56] F. A. Babushkin, Acta Phys. Pol. **25**, 749 (1964).

[57] D. Banaś, J. Braziewicz, A. Kubala-Kukuś, U. Majewska, M. Pajek, J. Semaniak, T. Czyżewski, M. Jaskóła, W. Kretschmer, and T. Mukoyama, Nucl. Instrum. Methods Phys. Res. B **164-165**, 344 (2000).

[58] J. L. Campbell and T. Papp, At. Data Nucl. Data Tables **77**, 1 (2001).

[59] D. Banaś, J. Braziewicz, M. Czarnota, M. Pajek, J. Semaniak, I. Fijał, M. Jaskóła, A. Korman, and W. Kretschmer, Nucl. Instrum. Methods Phys. Res. B **205**, 139 (2003).

[60] M. Czarnota, M. Pajek, D. Banaś, J.-Cl. Dousse, Y.-P. Maillard, O. Mauron, P. A. Raboud, M. Berset, D. Chmielewska, J. Rzadkiewicz *et al.*, J. Phys. Conf. Ser. **58**, 295 (2007).

[61] M. O. Krause, J. Phys. Chem. Ref. Data **8**, 307 (1979).

[62] M. H. Chen, B. Crasemann, and H. Mark, At. Data Nucl. Data Tables **24**, 13 (1979).

[63] M. H. Chen, B. Crasemann, and H. Mark, Phys. Rev. A **24**, 177 (1981).

[64] E. J. McGuire, *Atomic Inner-Shell Processes* (Academic, New York, 1975), p. 293.

[65] M. H. Chen and B. Crasemann, Phys. Rev. A **12**, 959 (1975).

[66] M. H. Chen, Phys. Rev. A **30**, 2082 (1984).

[67] F. P. Larkins, J. Phys. B **4**, L29 (1971).